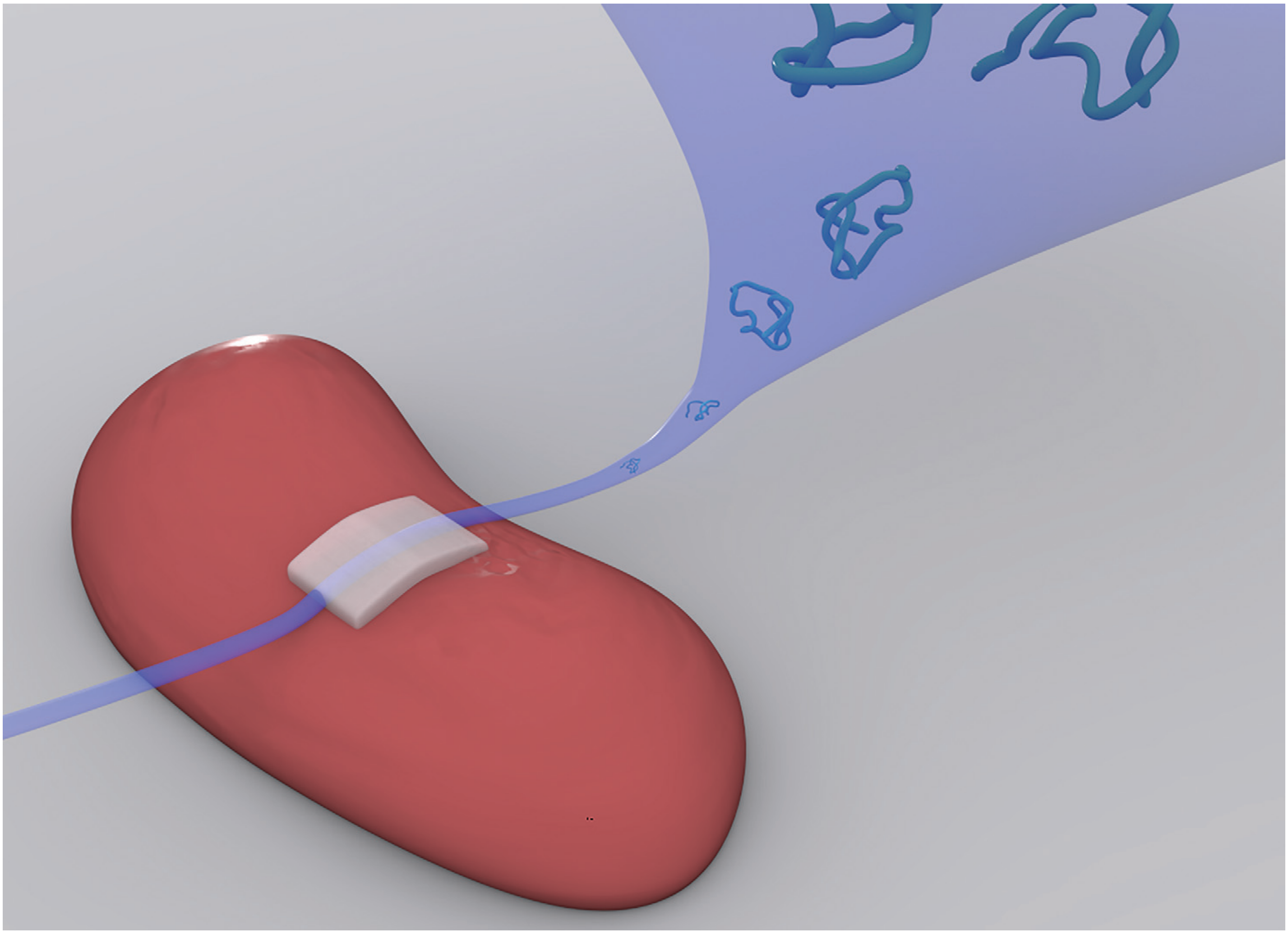

Featuring work from Professor Blake Johnson's Advanced Biomanufacturing and Biosensing Group at Virginia Tech.

3D printed conformal microfluidics for isolation and profiling of biomarkers from whole organs

3D Printing's Next Act – Conformal Microfluidics. 3D printed organ-conforming microfluidics now enable non-invasive, real-time isolation and profiling of biomarkers from whole organs. Conformal microfluidics appear poised to shift the paradigm for studying complex biological systems including 3D tissues and whole organs.

As featured in:

Lab on a Chip

See Blake N. Johnson *et al.*, *Lab Chip*, 2017, **17**, 2561.

ROYAL SOCIETY OF CHEMISTRY

rsc.li/loc

Lab on a Chip

PAPER

Cite this: *Lab Chip*, 2017, **17**, 2561

3D printed conformal microfluidics for isolation and profiling of biomarkers from whole organs†

Manjot Singh,‡[a] Yuxin Tong,‡[a] Kelly Webster,[g] Ellen Cesewski,[ad]
Alexander P. Haring,[ab] Sahil Laheri,[ac] Bill Carswell,[f] Timothy J. O'Brien,[ef]
Charles H. Aardema Jr.,[e] Ryan S. Senger,[fh]
John L. Robertson[ef] and Blake N. Johnson *[abcdh]

The ability to interface microfluidic devices with native complex biological architectures, such as whole organs, has the potential to shift the paradigm for the study and analysis of biological tissue. Here, we show 3D printing can be used to fabricate bio-inspired conformal microfluidic devices that directly interface with the surface of whole organs. Structured-light scanning techniques enabled the 3D topographical matching of microfluidic device geometry to porcine kidney anatomy. Our studies show molecular species are spontaneously transferred from the organ cortex to the conformal microfluidic device in the presence of fluid flow through the organ-conforming microchannel. Large animal studies using porcine kidneys (n = 32 organs) revealed the profile of molecular species in the organ-conforming microfluidic stream was dependent on the organ preservation conditions. Enzyme-linked immunosorbent assay (ELISA) studies revealed conformal microfluidic devices isolate clinically relevant metabolic and pathophysiological biomarkers from whole organs, including heat shock protein 70 (HSP-70) and kidney injury molecule-1 (KIM-1), which were detected in the microfluidic device as high as 409 and 12 pg mL^{-1}, respectively. Overall, these results show conformal microfluidic devices enable a novel minimally invasive 'microfluidic biopsy' technique for isolation and profiling of biomarkers from whole organs within a clinically relevant interval. This achievement could shift the paradigm for whole organ preservation and assessment, thereby helping to relieve the organ shortage crisis through increased availability and quality of donor organs. Ultimately, this work provides a major advance in microfluidics through the design and manufacturing of organ-conforming microfluidic devices and a novel technique for microfluidic-based analysis of whole organs.

Received 30th April 2017,
Accepted 12th June 2017

DOI: 10.1039/c7lc00468k

rsc.li/loc

Introduction

3D printing has enabled the creation of novel functional materials and devices containing diverse interwoven functional features.[1–7] Among these, 3D printing is revolutionizing the design and manufacturing of microfluidic devices in terms of materials flexibility,[8–10] biofunctionalization,[9] and microchannel design.[11,12] For example, heated microextrusion-based 3D printing has been used to construct low-cost microfluidic devices for carrying out a range of inorganic and organic chemical reactions.[10] In another study, stereolithography was used to fabricate microfluidic devices with channel sizes as small as 50 μm and internalized micro-mixing processes for time-resolved glucose detection.[11] Although conventional microfluidic devices contain 2D microfluidic networks, 3D printing was recently used to construct a microfluidic device that contained 3D helical microchannels for detection of pathogenic bacteria.[12] Given microfluidics form the basis for many biological technologies, these advantages of 3D printing, particularly the ability to construct novel 3D microchannel geometries, create unique opportunities for the development of novel microfluidic-based diagnostic and biomedical devices.

Recently, the ability to model complex biological systems using microfluidics has enabled paradigm shifting advances in the study of tissues and drug discovery.[13–15] The most common approach, known as the organ-on-a-chip concept, involves the

---

[a] *Department of Industrial and Systems Engineering, Virginia Tech, Blacksburg, VA 24061 USA. E-mail: bnj@vt.edu; Fax: 540 231 3322; Tel: 540 231 0755*
[b] *Macromolecules Innovation Institute, Virginia Tech, Blacksburg, VA 24061 USA*
[c] *School of Neuroscience, Virginia Tech, Blacksburg, VA 24061 USA*
[d] *Department of Materials Science and Engineering, Virginia Tech, Blacksburg, VA 24061 USA*
[e] *School of Biomedical Engineering and Sciences, Virginia Tech, Blacksburg, VA 24061 USA*
[f] *Department of Biological Systems Engineering, Virginia Tech, Blacksburg, VA 24061 USA*
[g] *Department of Mechanical Engineering, Virginia Tech, Blacksburg, VA 24061 USA*
[h] *Department of Chemical Engineering, Virginia Tech, Blacksburg, VA 24061 USA*

† Electronic supplementary information (ESI) available. See DOI: 10.1039/c7lc00468k

‡ These authors contributed equally to this work.

direct seeding of cells into the microchannels of microfluidic devices. For example, to date, organ-on-a-chip platforms have been created for a variety of organs, including the lung,[16] liver,[17] and nervous system.[9] However, although highly advantageous from a number of perspectives (*e.g.* high throughput), such microfluidic-based *in vitro* models require the removal of cells from their native *in vivo* environments and are not applicable to the analysis of whole organs. Thus, the ability to interface microfluidic devices directly with whole organs could both complement present organ-on-a-chip technology, as well as usher in a novel paradigm for the study and analysis of organs. However, such a paradigm hinges on the ability to coherently integrate microfluidic devices and whole organs. Importantly, given 3D printing enables microfluidic device manufacturing and exhibits compatibility with conformal manufacturing and medical imaging technology,[1,4,18–21] 3D printing appears poised to create next-generation microfluidic devices for whole organ healthcare (*e.g.* organ assessment).

Organ failure is the most common cause of morbidity and mortality.[22–24] Although transplantation saves the lives of patients with organ failure, there is a critical shortage of donor organs.[22] Among the various challenges that underlie the organ shortage crisis,[25,26] the inability to monitor the molecular trajectories of whole organs throughout the clinically relevant ischemic interval constrains our ability to objectively assess organ quality,[27] thereby limiting donor organ availability and transplant efficacy. For example, a high number of potentially useful organs (*e.g.*, from extended criteria donors) are discarded due to subjectively perceived inferior function.[28,29] Additionally, preservation under sub-optimal conditions (due to limited understanding of the ischemic mechanisms that govern transplantation outcome) may foster organ deterioration.[27] It was recently reported that unique molecular trajectories become active after organism death,[30] suggesting that assessing the dynamic molecular trajectories of whole organs throughout the ischemic interval may have value. Unfortunately, the characteristics of such trajectories, and value thereof, are presently unknown due to a lack of integrative biotechnology capable of continuously isolating molecular species from organs in a transplantation setting. Thus, a technique for monitoring the molecular profiles and trajectories of whole organs throughout the clinically relevant ischemic interval could help relieve the organ shortage crisis.

Here, we demonstrate a bio-inspired microextrusion 3D printing approach for the design and manufacturing of organ-conforming microfluidic devices. Structured-light scanning enabled the 3D topographical matching of microfluidic device geometry to organ anatomy. We show that conformal microfluidic devices provide a novel approach for real-time isolation and profiling of molecular species from whole organs, which we refer to as 'microfluidic biopsy'. In contrast to traditional biopsy, microfluidic biopsy *via* organ-conforming microfluidic devices involves no tissue removal, provides dynamic information throughout a clinically relevant interval, and offers real-time monitoring capabilities. For the first time, we show that fluid samples acquired *via* organ-conforming microfluidic devices (*i.e.* microfluidic biopsy samples) contain clinically relevant metabolic and pathophysiological biomarkers, and thus, have significant diagnostic value for objective organ assessment. Analysis of the microfluidic biopsy samples also shows that the dynamic molecular trajectories of whole organs depend on preservation conditions. Ultimately, we believe that organ-conforming microfluidic devices will enable biotechnological breakthroughs for the study and analysis of whole organs. As a result, this work provides a disruptive microfluidic-based technology and a novel approach to organ assessment that may help relieve the organ shortage crisis.

Materials and methods

2.1 Materials

Phosphate buffered saline (PBS) and Pluronic F-127 were from Sigma Aldrich. Sodium polyacrylate hydrogel was from Hollister. Silicone (SI 595 CL) was from Loctite. Enzyme-linked immunosorbent assay (ELISA) kits for porcine heat shock protein 70 (HSP-70), kidney injury molecule-1 (KIM-1) and β-actin were from Elabscience. Ultrapure de-ionized water (DIW) was obtained from a commercially available DIW system (Direct-Q 3UV; Millipore).

2.2 Organ procurement and preservation

Adult female porcine kidneys were procured from a local abattoir. Animals were euthanized and handled in strict accordance with good animal practice as defined by the relevant national and local animal welfare bodies, and approved by Virginia Tech. Kidneys were procured by first removing the viscera *en bloc*. Subsequently, the kidneys were dissected from the viscera. Kidneys were separated into three experimental groups: a normothermic group (n = 19 organs), a traditional cold storage hypothermic group (n = 6 organs), and a machine-perfused hypothermic group (n = 7 organs). Organs from the normothermic group were procured and subsequently stored in an insulated container during transportation to the assessment site. Organs from the traditional cold storage hypothermic group were procured and subsequently stored on ice in an insulated container during transportation to the assessment site. Organs from the machine-perfused hypothermic group were procured and subsequently stored on ice in an insulated container during transportation to the assessment site where they were then anastomosed to an organ preservation system. The transportation time was *ca.* 2 hours. All organs were procured from different animals, except for the six organ pairs (n = 12 organs total) that were used for the traditional cold storage hypothermic group *vs.* normothermic group paired organ study, which were procured as paired organs from the same animal. Paired organ studies were conducted by subjecting paired organs from the same animal to different ischemic conditions to control for animal-to-animal variance in organ pathophysiology. Prior to machine perfusion studies, the renal vein, artery, and ureter were fitted with Luer Lock connectors. Kidneys from the machine-perfused hypothermic group were anastomosed to a hypothermic organ preservation system that provided a sinusoidal pressure waveform. The kidneys were perfused with PBS (T = 4 °C) using a sinusoidal pressure waveform (90/60 mmHg). Photographs of the machine perfusion system and the microfluidic biopsy measurement are shown in Fig. S1 and S2 of ESI,† respectively.

2.3 Reverse engineering of organ geometry *via* structured-light scanning

Kidneys were prepared for imaging by removing excess fatty tissue from the hilus and carefully suturing the fatty tissue with a suture line for suspension. Kidneys were then suspended in a 38% ethanol solution (v/v in water) by the suture lines and subsequently stored at *ca.* −15 °C overnight. The frozen kidneys were then suspended on an articulating arm boom stand (HP 3D Desk Scan Lever Pro; HP) by the suture lines, which allowed the tissue to be imaged from various vantage points over a full rotational angle. The kidneys were subsequently imaged using a single camera-projector structured-light scanning system (HP 3D Structured Light Scanner Pro S2; HP). Prior to imaging, the system was calibrated following vendor-provided protocols using a 60 mm calibration grid. Kidneys were imaged by performing multiple scans over a 360° rotational angle. Following scanning, the raw scan data in the form of individual point cloud files were subsequently aligned using data alignment functions of the vendor-provided software, which resulted in a water-tight 3D model of the kidney. The above protocol was repeated using multiple organs from randomly selected animals in order to simulate application in the point-of-care and account for inherent animal-to-animal variance.

2.4 3D printing of organ-conforming microfluidic devices

Models of whole kidneys were first printed based on the digitized kidney data using a commercially-available plastic 3D printer (Printrbot Simple Metal; Printrbot) to provide biomimetic substrates for conformal printing. The organ-conforming microfluidic devices were then printed on the biomimetic substrates using a custom microextrusion-based 3D printing system, which has been described previously.[4–6,18] The system consisted of a three-axis industrial dispensing robot (F5200N; Fisnar), digital pressure regulator (Ultimus V; Nordson), and a custom imaging system (see Fig. S3 of ESI†). Path information for the conformal microfluidic devices was constructed based on the 3D organ surface topographical data acquired by structured-light scanning. Conformal microfluidic devices were printed using silicone with a 16–20 gauge tapered tip, extrusion pressure of 10 psi, and printing speed of 2 mm s^{-1}. The build time was *ca.* one hour. Following printing, the devices were cured, released from the organ substrate, and sterilized with ethanol spray. To provide an adhesion layer for bonding to whole organs, the 3D surface topographical data was subsequently used to apply a thin hydrogel layer (sodium polyacrylate or 30 wt% Pluronic F-127) across the device's organ contact surface, with the exception of the microchannel. Hydrogel 3D printing was done using a 27 gauge tapered tip (Nordson EFD), extrusion pressure of 12 psi, and printing speed of 1 mm s^{-1}. The build time was *ca.* 30 minutes. Subsequently, hollow pins were inserted into the microchannel inlet and outlet to provide interface with external fluid handling supplies and instrumentation (*i.e.*, tubing, syringe pump and sample collection reservoir).

2.5 3D Topographical analysis

Topographical data for comparison of the 3D printed conformal microfluidic device and organ curvature were obtained using structured-light scanning. 3D printed conformal microfluidic devices were first mounted vertically on a flat substrate. Subsequently, the devices were coated with a thin film of contrast agent (Magnaflux). Prior to imaging, the system was calibrated following vendor-provided protocols using a 30 mm calibration grid. The devices were then scanned and water-tight 3D models were generated as described for structured-light scanning of kidneys. The point cloud data of the kidney and device surfaces corresponding to the organ-device interface location were first isolated. Subsequently, a 0.2 mm wide band across each data set was isolated. The coordinates from each data set were then processed using the following approach to extract the topographical curvature (*i.e.*, the curvilinear coordinate lines). Using the organ data set as a basis, the coordinates from the device data set were first rotated through a rotation matrix until the unit normal vector at the center of the device coordinate line aligned with the unit normal vector at the center of the organ coordinate line. Subsequently the coordinate lines were shifted into the first quadrant by linearly transforming each set. Non-conformal microfluidic devices printed on flat substrates served as a control for comparing the device-organ 3D topographical matching. The data from control devices was analyzed identically to the conformal microfluidic devices.

2.6 Microfluidic biopsy

The inlet pin of the conformal microfluidic device was first connected to a syringe pump. Prior to interfacing the 3D printed conformal microfluidic device with the kidney, an incision was made in the kidney's capsule at the lateral border, which coincided with the same location used for reverse engineering of anatomical device geometry, to create a 3 × 3 cm^2 flap that could be lifted to expose the renal cortex. Subsequently, the device was manually applied to the renal cortex at the scanned location. Two trans-channel microneedles (27 gauge) were then inserted through the top of the device and *ca.* 5 mm into the lateral border along the channel length. PBS (10 mM; pH 7.4) was then introduced to the device at a flow rate of 100 μL min^{-1}. The outlet fluid, referred to as the microfluidic biopsy sample, was continuously collected in 1.5 mL aliquots. Given a desirable clinically relevant assessment interval is approximately one hour, the microfluidic biopsy samples collected at $t = 1$ hour (independent of previously collected aliquots) were analyzed using Raman spectroscopy and enzyme-linked immunosorbent assay (ELISA). The aliquots collected prior to one hour were not assessed, but were collected to demonstrate the potential for temporal assessment.

2.7 Raman spectroscopy

Molecular cluster analysis (*i.e.*, bio-fingerprinting) of microfluidic biopsy samples was conducted using Raman spectroscopy (Desktop H-PeakSeeker; Agiltron) and methodology established in the literature.[31] The Raman spectrum of each sample was collected using vendor-provided software (RSIQ) over 250–1950 cm^{-1} with a step size of 1 cm^{-1} using a 785 nm laser. Ten scans were conducted per sample. Scans were collected with integration and delay times of 15 s (see Fig. S4 of ESI† for representative Raman spectra). After data collection, all microfluidic biopsy sample scans were vector normalized and statistically analyzed using principal component analysis (PCA) and then linear discriminant analysis of principal components (DAPC). The number of principal components used in DAPC accounted for 90% of the variance in the dataset. The Raman molecular clustering profile was subsequently visualized by plotting the first two canonicals of DAPC (*e.g.*, canonical 1 and canonical 2). *P*-Values (p) associated with the statistical significance of differences between the means of the cluster location (*i.e.*, mean canonical coordinates for a given experimental group) were calculated using a two-tailed Student's *t*-test assuming unequal variances.

2.8 Enzyme-linked Immunosorbent assay (ELISA)

The concentrations of HSP-70, KIM-1, and β-actin in the microfluidic biopsy samples were quantified using commercially-available ELISA kits according to vendor-provided protocols. Briefly, a standard solution was first serially diluted over the ng mL^{-1}–pg mL^{-1} range. Subsequently, 100 μL of standard, microfluidic biopsy sample, or control was added to each well and incubated for 90 minutes at 37 °C. The liquid was then removed, each well was washed, and 100 μL of biotinylated detection antibody was added to each well and incubated for one hour at 37 °C. The liquid from each well was then aspirated and each well was washed with wash buffer. Subsequently, 100 μL of horseradish peroxidase conjugate was added and incubated for 30 minutes at 37 °C. The liquid from each well was again aspirated and the well was washed with wash buffer. Following the wash step, 90 μL of substrate reagent was added and incubated for 15 minutes at 37 °C. Next, 50 μL of stop solution was added and the absorbance of the microplates were read at 450 nm. All microplates were analyzed using a multi-mode fluorescence microplate reader (Synergy H1m; BioTek). The average absorbance value for each experimental organ group (*i.e.*, normothermic (NT), traditional cold storage hypothermic (HT), and machine-perfused hypothermic (HT-P)) and the negative control (Neg) group was then calculated. A standard curve was created by plotting the absorbance value at each concentration of the serially diluted standard on a semi-log plot and fitting a linear best-fit curve to the data. The protein concentration in the experimental samples was then obtained using the average absorbance value and the calibration curve, and subsequent scaling based on the internal controls. *P*-Values (p) associated with the statistical significance of differences between the mean concentration of experimental groups were calculated using a two-tailed Student's *t*-test assuming unequal variances.

2.9 Computational fluid dynamics and convective mass transfer simulations

All studies were performed using commercially available finite element analysis (FEA) software (COMSOL Multiphysics, Version 5.2 a). Stationary studies were conducted in 3D using the Laminar Flow interface within the Fluid Flow module (Single Batch Phase Flow) and the Transport of Diluted Species interface within the Chemical Species Transport module. The computational domain was created using the graphics-user interface based on the structured-light scanning-generated topography of the 3D printed microfluidic channel. Simulations were done assuming Newtonian and Fickian constitutive relations. The material properties were taken from published literature (density of water[32] = 997 kg m^{-3}; dynamic viscosity of water[32] = 8.9×10^{-4} Pa s; diffusivity of HSP-70 in water[33] = 10^{-10} $\text{m}^2\ \text{s}^{-1}$; molecular weight of HSP-70[34] = 70 kDa; concentration of HSP-70 in normothermic kidney tissue[35] = 275 ng mL^{-1}). The boundary conditions for the fluid flow problem included a normal mass flow rate condition at the inlet, an atmospheric pressure condition at the outlet (normal flow), and no-slip conditions along the channel walls. The boundary condition for the mass transfer problem included a zero concentration condition at the inlet, insulation (*i.e.*, no flux) conditions along the channel walls, and an overriding mass flux condition along the bottom wall of the microchannel that is formed by the organ surface at the trans-channel microneedle locations. The mass flux (j) was modelled using a form of Newton's Law of Cooling for internal flow:[36]

$$j = k(c_\text{s} - c_\text{m}) \tag{1}$$

where k is the convective mass transfer coefficient, c_s is the surface concentration, and c_m is the mean (or bulk) fluid concentration at a given cross section. The value of c_s was obtained from published literature on the concentration of HSP-70 in kidney tissue (275 ng mL^{-1})[35] and the molecular weight of HSP-70 (70 kDa).[34] The mean fluid concentration was assumed to be far less than the surface concentration (*i.e.*, $c_\text{m} \ll c_\text{s}$), and thus, was assumed to be zero in the calculation of the mass flux (an assumption that is supported by the simulation results; see section 2 of ESI†). We used a corrected empirical convective mass transfer correlation for internal laminar flow in circular tubes subjected to a constant surface concentration condition developed by Sieder and Tate to calculate the convective mass transfer coefficient:[36]

$$\overline{Sh} = c_{\mathrm{f}} 1.86 \left(\frac{ReSc}{L/D_{\mathrm{h}}}\right)^{1/3} \left(\frac{\mu}{\mu_{\mathrm{s}}}\right)^{0.14} \tag{2}$$

where $\overline{Sh} = kL/D$ is the average Sherwood number, μ_s is the dynamic viscosity of the fluid at the surface and c_f is a correction factor = 4.36/3.66.[36] See section 2 of ESI† for a detailed discussion of convective mass transfer modelling. Initial values corresponded to zero velocity, pressure, and concentration fields across the entire domain. The model was discretized using a physics-controlled mesh (finer element size), which consisted of 849 802 domain, 71 710 boundary, and 2209 edge elements. The shear rate and concentration profiles were calculated using a stationary solver. An auxiliary sweep was conducted to calculate the shear rate and concentration profiles over a range of flow rates (20–200 μL min^{-1}) with a step size of 20 μL min^{-1}. The outlet velocity, mean concentration, and average shear rate along the bottom wall (*i.e.*, the organ surface) were calculated as derived quantities from these results. Proper density of the mesh was checked by examining convergence of the outlet velocity and concentration by iterating from a coarse to an extra fine mesh element size, which led to convergence within less than 0.05 and 3.5% of the previous mesh iterate, respectively.

Results and discussion

3.1 Topographical matching of 3D printed conformal microfluidic devices with organ anatomy

The renal cortex is the most metabolically active region of the kidney and performs critical physiological processes, such as ultrafiltration. Thus, we have focused on microfluidic biopsy of the renal cortex as we hypothesize it contains rich diagnostic information, such as biomarkers of ischemic pathophysiology, that can be used to objectively assess organ quality within the clinically relevant ischemic interval (*e.g.*, by transplantation surgeons). As shown schematically in Fig. 1, we leveraged a bio-inspired conformal 3D printing approach to fabricate anatomical organ-conforming microfluidic interfaces capable of isolating molecular species from the renal cortex, which we refer to as 'microfluidic biopsy'. As shown by the last panel of Fig. 1, the microfluidic biopsy concept is founded on the spontaneous transfer of biomarkers from the organ cortex to an adjacent microfluidic stream established by the 3D printed organ-conforming microfluidic device. Thus, analyzing the outlet fluid of the organ-conforming microfluidic device, referred to as the microfluidic biopsy sample, potentially enables the real-time monitoring of whole organ molecular trajectories (*e.g.*, molecular profiles and biomarker expression levels).

As shown in Fig. 2a, we first digitized whole kidneys using structured-light scanning to both generate 3D surface topography data required for conformal manufacturing and create a biomimetic substrate for conformal 3D printing (see Fig. S3†). Following the reverse engineering process, microfluidic devices were printed directly on the biomimetic substrates. Fig. 2b highlights the resultant 3D printed organ-conforming microfluidic device used for microfluidic biopsy. As shown in Fig. 2c, the conformal microfluidic devices could be effectively interfaced with explanted kidneys and supporting fluid handling components (see Fig. S5–S7 of ESI† for additional photographs of device manufacturing, device geometry, and organ interface).

Having shown the ability to manufacture microfluidic devices on biomimetic substrates, we next verified the topographical matching between the 3D printed microfluidic device and the organ anatomy at the interface location (the lateral border of the kidney). As shown in Fig. 2d, the curvilinear coordinate lines of the device and organ surface exhibited topographical alignment, thereby confirming device-organ coherence (see Fig. S6 of ESI† for topographical comparison with a non-conforming negative control device). The collective data in Fig. 2a–d show proof-of-principle for fabrication and interface of 3D printed conformal microfluidic devices with whole organs, thereby providing the opportunity to establish controlled fluid flow across the organ cortex and collect microfluidic biopsy samples.

3.2 Computational analysis of fluid mechanics in 3D printed conformal microchannels

Given the microfluidic biopsy concept is founded on the spontaneous transfer of molecular species from the organ cortex into

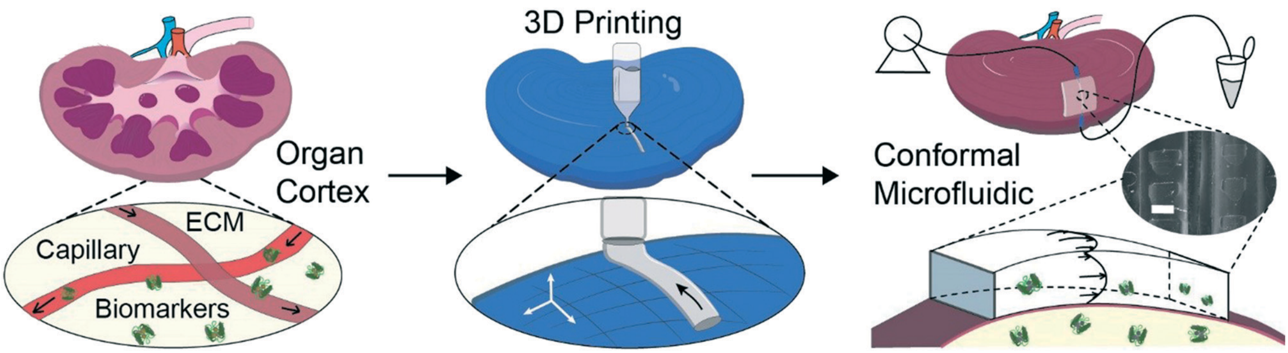

Fig. 1 Schematic of the microfluidic biopsy concept for isolating biomarkers from the cortex of whole organs using 3D printed conformal microfluidic devices (scale bar = 500 μm).

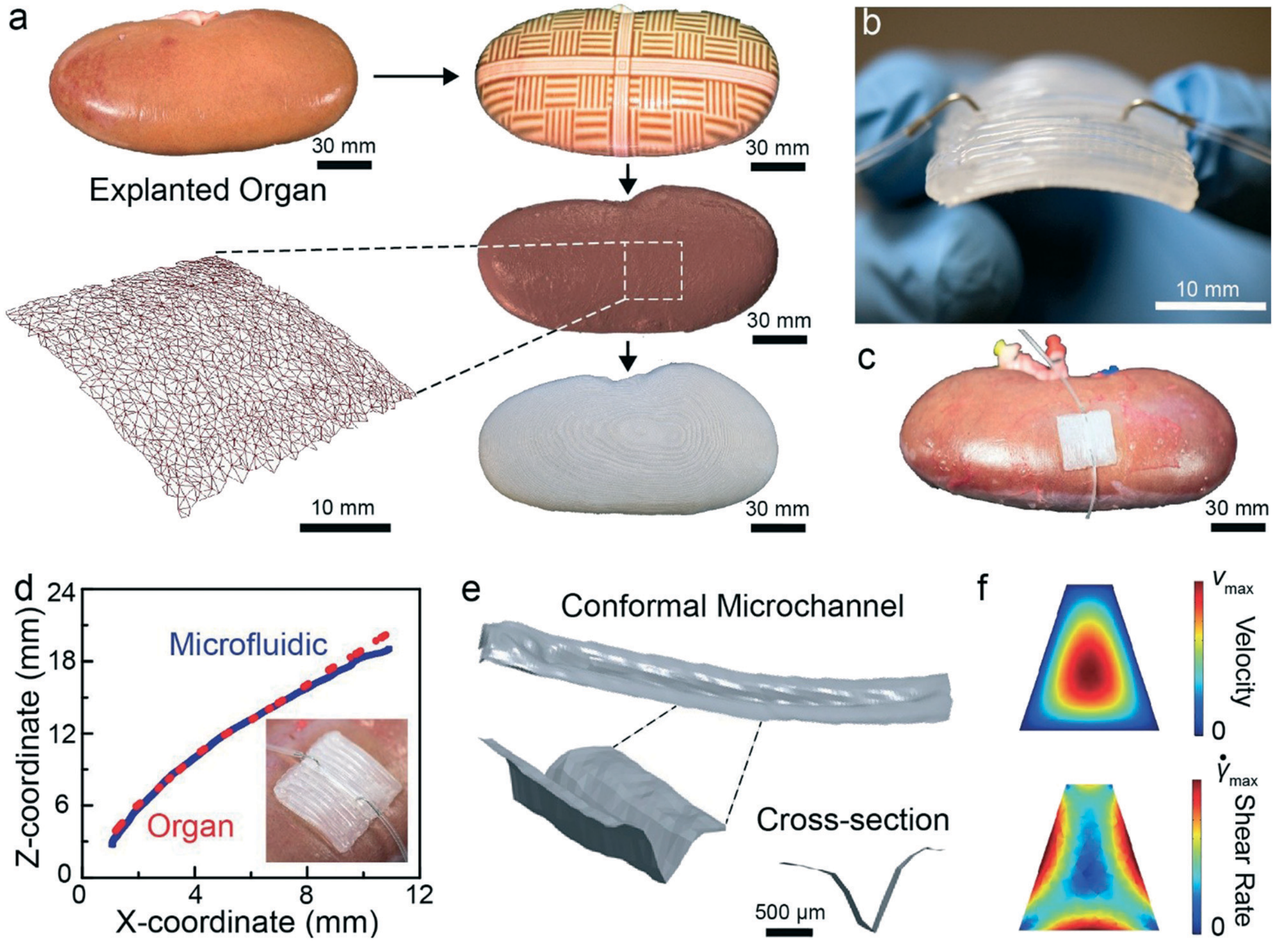

Fig. 2 3D printed organ-conforming microfluidic devices for whole organ microfluidic biopsy. a) Reverse engineering process for converting anatomical geometry of whole organs into both 3D printer path information and biomimetic substrates for 3D printing (shown in order are an explanted kidney, a kidney exposed to structured-light, a reconstructed digital model of the kidney, and a 3D printed model of the kidney; the expanded region shows the digitized 3D surface topography at the device interface location). b) Photograph of a 3D printed conformal microfluidic device. c) Photograph of a 3D printed conformal microfluidic device interfaced with a kidney. d) Topographical comparison between the organ and the 3D printed conformal microfluidic device at the interface location (inset shows close up view of the device-organ interface). e) 3D topographical characterization of the 3D printed conformal microchannel. f) Fully developed velocity and shear rate profiles present in the 3D printed conformal microfluidic device.

an adjacent microfluidic stream established by the organ-conforming microfluidic device, we next characterized the 3D topography and flow characteristics of the conformal microfluidic channel. As shown in Fig. 1, the 3D printed conformal microfluidic device contains an open basal microchannel. Thus, application of the conformal microfluidic device to the organ establishes a sealed microchannel in which the bottom surface is formed by the organ cortex. We next used structured-light scanning to characterize the 3D topography of the conformal microchannel. As shown in Fig. 2e, the conformal microchannel exhibited a trapezoidal cross-section to maximize the organ contact area and showed identical topographical matching to the device-organ contact surfaces. The hydraulic diameter of the conformal channel was 600 μm. Having characterized the 3D topography of the printed conformal microchannel, we next examined the flow characteristics in the device using 3D computational fluid dynamics (CFD) studies. Our studies revealed the organ cortex (*i.e.*, the microfluidic biopsy location) contacts a microfluidic stream that has a fully developed velocity profile along the majority of the microchannel ($L \sim 15$ mm). Fig. 2f shows the fully developed velocity and shear rate profiles in the conformal microchannel. Such a result is consistent with the theoretical hydrodynamic entry length for internal laminar flow, which predicts the velocity profile becomes fully developed after ~140 μm (see section 2 of ESI†). The average shear rate across the organ cortex changes linearly from 18–183 s^{-1} over a 20–200 μL min^{-1} flow rate range, respectively. Detailed descriptions of the computational domain and CFD studies are presented in Fig. S8 and S9 of ESI.† Experimentally, we found the device could operate effectively over a 1–100 μL min^{-1} flow rate range (flow rates beyond this range were not examined). Collectively, the data shown in Fig. 2 demonstrate that 3D printed conformal microfluidic devices form coherent interfaces with whole organs and can establish controlled fluid flow across the organ cortex, thus serving as a potential sink for continuously isolating molecular species.

3.3 Molecular cluster profiling of isolated microfluidic biopsy samples under different organ preservation conditions

Having demonstrated the ability to interface conformal microfluidic devices with whole organs and establish flow across the 3D organ cortex, we next examined if molecular species from the organ cortex spontaneously transfer into the organ-conforming microfluidic stream. Toward this objective, we conducted large animal studies that explored the effect of ischemic conditions on the molecular trajectory of whole organs throughout the clinically relevant ischemic interval using the microfluidic biopsy technique. As shown schematically in Fig. 3a, our first study investigated the molecular clustering profiles from kidneys exposed to normothermia (NT) and traditional cold storage hypothermia (HT). Photographs of the 3D printed conformal microfluidic device and schematic of the microfluidic biopsy principle are shown in Fig. 3b. As shown in Fig. 3b and S10,† the hydrogel adhesion layer provides a watertight seal between the organ surface and the 3D printed conformal microfluidic device (see Video S1 of ESI†). Thus, both the roughness variations between the organ and the 3D printed

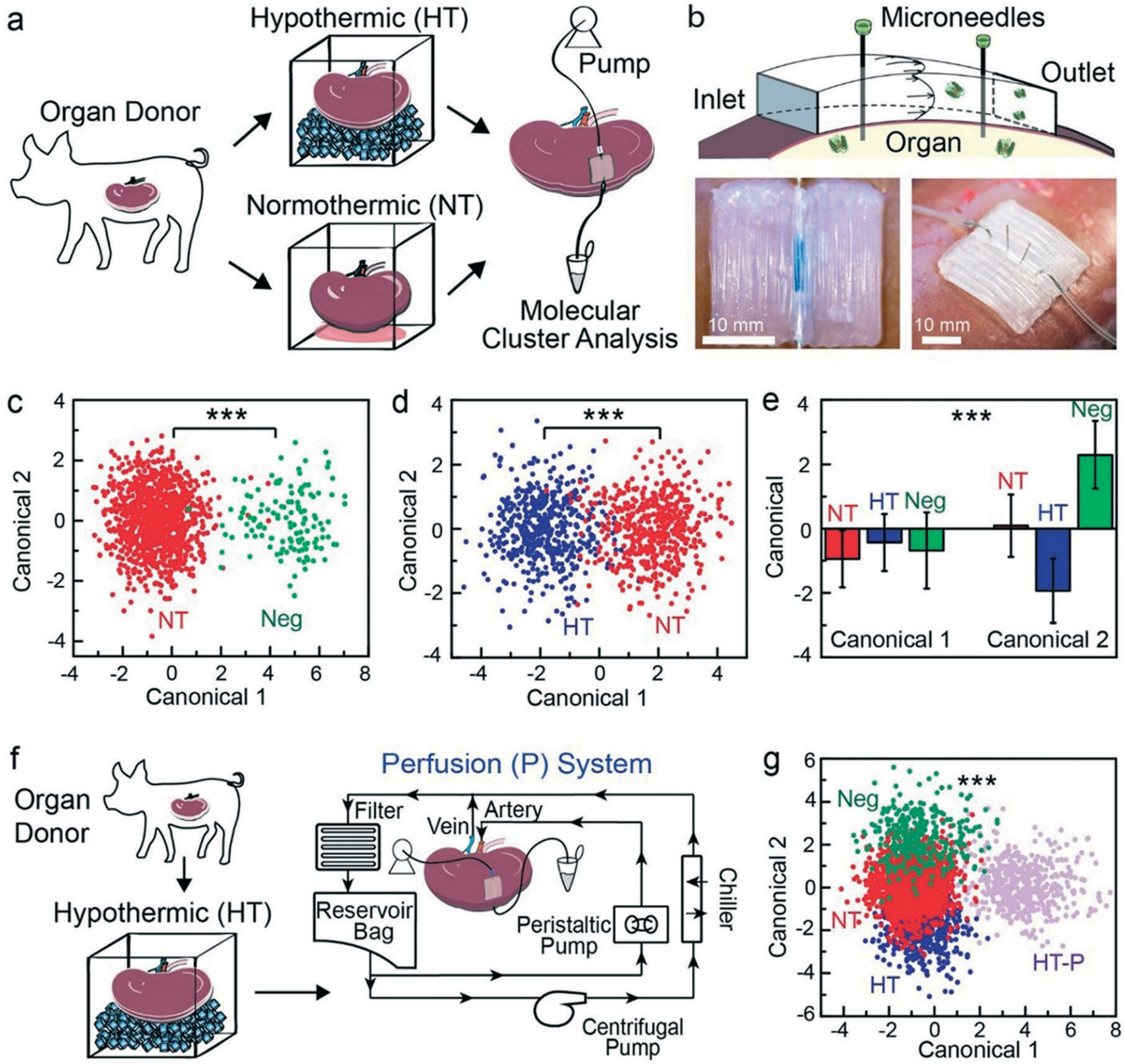

Fig. 3 Isolation and profiling of molecular species from whole organs under diverse ischemic conditions *via* 3D printed conformal microfluidic devices. a) Schematic of the large animal study for testing the effect of ischemic conditions on the molecular clustering profiles of microfluidic biopsy samples. b) Schematic and photographs of the 3D printed conformal microfluidic device used for microfluidic biopsy showing the isolation principle, the microchannel pathway (blue dye), and integration of trans-channel microneedles. c) Molecular cluster analysis comparing microfluidic biopsy samples acquired from organs subjected to normothermia (NT) *vs.* a negative control (Neg). d) Molecular cluster analysis comparing microfluidic biopsy samples acquired from paired organs subjected to either normothermia (NT) or traditional cold storage hypothermia (HT). e) Comparison of molecular clustering profiles among all organs subjected to normothermia, traditional cold storage hypothermia, and negative controls. f) Schematic of the large animal machine perfusion study for testing the effect of hypothermic ischemic conditions on the molecular clustering profiles of microfluidic biopsy samples. g) Comparison of molecular clustering profiles among all organs subjected to normothermia (NT), traditional cold storage hypothermia (HT), machine-perfused hypothermia (HT-P), and negative controls (Neg). Triple asterisks indicates $p < 0.001$ among all clusters.

device caused by layer-by-layer 3D printing artifacts and the position uncertainty caused by manual placement are within the tolerance level of the device.

Trans-channel microneedles were inserted into the renal cortex prior to establishing fluid flow and remained throughout the experiment to support the spontaneous transfer of biomarkers into the fluid channel such that the concentration of biomarkers in the microchannel could be detected by Raman spectroscopy or ELISA. We first conducted control studies by comparing the molecular clustering profiles of microfluidic biopsy samples acquired from the normothermic group (n = 13 organs) with a control (Neg) group that consisted of input saline solution (n = 13 samples). As shown in Fig. 3c, the molecular clustering profiles of the normothermic group and the control group exhibited statistically significant differences in the center of mass (CM) location in the two-dimensional canonical plane. For example, the CM for the normothermic group and the control group was located at (−0.59, 0) and (4.71, 0), respectively ($p < 0.001$; number of points per cluster (n_{points}) = 1040 and 130, respectively). Given the only difference between the samples in each group was exposure to the renal cortex, the results suggest that molecular species are spontaneously transferred from the renal cortex to the organ-conforming microfluidic stream. Thus, we next compared the molecular clustering profiles of microfluidic biopsy samples acquired from the normothermic group with the traditional cold storage hypothermic group using a paired organ study (see Fig. 3a). Importantly, Fig. 3d shows the molecular clustering profiles of the normothermic group (n = 6 paired organs) and traditional cold storage hypothermic group (n = 6 paired organs) exhibited statistically significant differences in CM location. For example, the CM for the normothermic group and the traditional cold storage hypothermic group was located at (1.84, 0) and (−1.84, 0), respectively ($p < 0.001$; n_{points} = 480 for each cluster). Given the only difference between the samples in each group was the ischemic conditions, as the use of paired organs controlled for animal-to-animal variations, the results suggest that the molecular trajectories of whole organs depend on the ischemic conditions. As shown in Fig. 3e, distinctive clustering of normothermic and traditional cold storage hypothermic groups was also observed when examining microfluidic biopsy samples acquired from both paired and non-paired organs (n = 25 organs total; n = 32 negative control samples; $p < 0.001$; n_{points} = 1520, 480, and 320 for the normothermic, traditional cold storage hypothermic, and negative control groups, respectively). In order to examine the sensitivity of the molecular clustering profile (*i.e.*, the population of isolated molecular species) to variations in the ischemic conditions, as shown schematically in Fig. 3f, we next acquired microfluidic biopsy samples from organs that were subjected to machine perfusion throughout the hypothermic ischemic interval (see Fig. S1, S2, and S10 of ESI† for details on the experimental setup). As shown in Fig. 3g, the molecular clustering profile of the machine-perfused hypothermic group (n = 7 organs) exhibited a statistically significant difference in CM location from the traditional cold storage hypothermic group as well as the normothermic and control groups. For example, the CM for the normothermic group, the traditional cold storage hypothermic group, the machine-perfused hypothermic group, and the negative control group was located at (−0.94, 0.09), (−0.43, −1.93), (3.87, 0.12), and (−0.68, 2.30), respectively ($p < 0.001$; n_{points} = 1520, 480, 480, and 320, respectively). The results in Fig. 3 indicate multiple critical findings: 1) the microfluidic biopsy technique provides a novel approach for isolating molecular species from the renal cortex; 2) the populations of isolated molecular species depend on the ischemic conditions; 3) whole organs exhibit dynamic molecular trajectories throughout the ischemic interval; and 4) the microfluidic biopsy technique enables monitoring of whole organ molecular trajectories throughout the clinically relevant ischemic interval.

3.4 Computational modeling of biomarker mass transfer in organ-conforming microfluidic devices

The results in Fig. 3 show that molecular species can be isolated from whole organs using the novel microfluidic biopsy technique and the profile of isolated molecular species depends on the ischemic conditions (*i.e.*, the preservation conditions). Thus, we next examined if the population of isolated molecular species isolated by the organ-conforming microfluidic device contained biomarkers that hold diagnostic value for organ assessment, such as biomarkers of metabolic activity and ischemic pathophysiology. We first modeled the mechanism of microfluidic biopsy (*i.e.*, spontaneous transfer of biomarkers from the organ cortex to the organ-conforming microfluidic stream) using a 3D multiphysics model to inform and interpret the subsequent bioassay. As shown schematically in Fig. 4a, the penetration of trans-channel microneedles into the organ cortex can be modeled as a localized zone for spontaneous transfer of molecular species from the organ cortex to the microfluidic stream. The corresponding steady state 3D concentration profile in the conformal microfluidic device during a microfluidic biopsy measurement is shown in Fig. 4b. Fig. 4c highlights the concentration profile at various cross sections along the microchannel. In contrast to the velocity profile, the calculations show that the concentration profile does not become fully developed prior to reaching the microfluidic outlet. Such a result is consistent with the theoretical thermal entry length for internal laminar flow (see section 2 of ESI†), which predicts the concentration profile requires 1.27 m to become fully developed. Given the trans-channel microneedles establish a non-uniform axial flux boundary condition along the organ cortex, it was of interest to examine the mean fluid concentration along the microchannel (details of the flux boundary condition are provided in section 2 of ESI†). As shown in Fig. 4d, two concentration 'hot-spots' are observed at 5.5 and 10.75 mm, which coincide with the location of the flux boundary condition (*i.e.*, microneedle location). The hot-spot

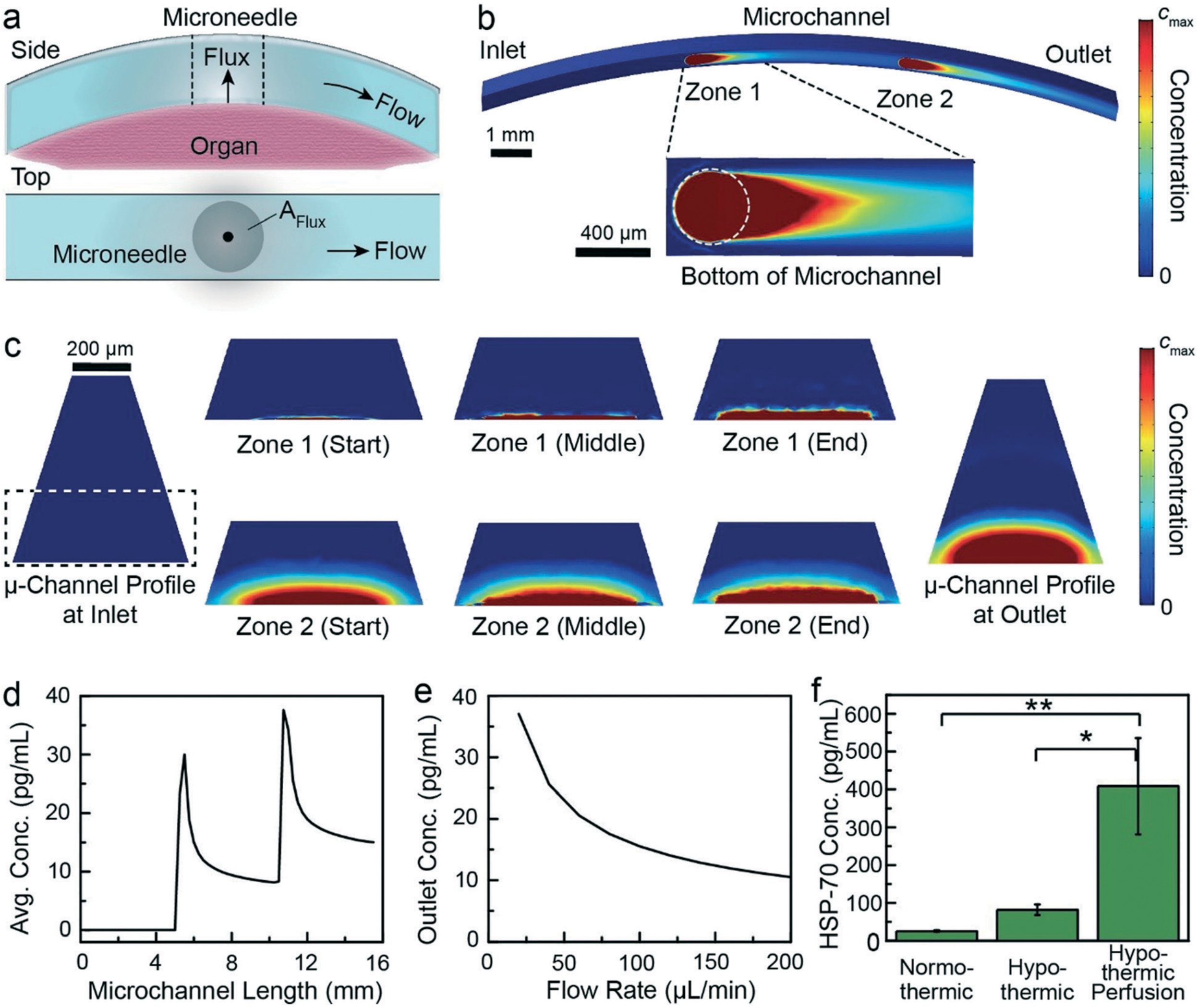

Fig. 4 Identification and quantification of biomarkers of ischemic pathophysiology and metabolic activity in microfluidic biopsy samples. a) Schematic of the microfluidic biopsy mechanism showing the localization of mass flux boundary conditions along the microchannel. b) 3D concentration profile in the conformal microfluidic channel highlighting concentration "hot-spots" caused by trans-channel microneedles (white circle shows the microneedle dimensions). c) 2D concentration profiles along the microchannel (white box shows the channel region corresponding to the shown concentration profiles across the two hot-spot zones). d) Mean (or bulk) fluid concentration of biomarkers in the microchannel along the length of the microchannel. e) Mean outlet fluid concentration of biomarkers in the 3D printed conformal microfluidic device (*i.e.*, concentration of the microfluidic biopsy sample) *vs.* flow rate (experimental flow rate = 100 µL min^{-1}). f) Comparison of the heat shock protein 70 (HSP-70) levels found in microfluidic biopsy samples collected from organs exposed to normothermia, traditional cold storage hypothermia, and machine-perfused hypothermia. Single and double asterisks indicate $p < 0.05$ and $p < 0.01$, respectively.

phenomenon has been previously reported in heat transfer problems involving analogous non-uniform axial flux boundary conditions.[37,38] Fig. 4e shows the dependence of the mean fluid outlet concentration (*i.e.*, the concentration of the microfluidic biopsy sample) on flow rate through the microfluidic device. As shown in Fig. 4e, the concentration of the microfluidic biopsy sample changed nonlinearly from 37–11 pg mL^{-1} over a 20–200 µL min^{-1} flow rate range, respectively. At the experimental flow rate (100 µL min^{-1}), the predicted concentration of the microfluidic biopsy sample was 16 pg mL^{-1}. Thus, the results shown in Fig. 4d and e suggest that biomarkers should be detectable in microfluidic biopsy samples using ELISA without the need for sample preparation steps (*e.g.*, dilution or enrichment).

3.5 Identification and quantification of biomarkers in microfluidic biopsy samples

Various biomarkers have been identified in circulating body fluids and organ tissue as diagnostic tools for kidney transplantation *via* blood and urine analysis and traditional biopsy techniques, respectively.[39] Among these, heat shock protein 70 (HSP-70) and kidney injury molecule-1 (KIM-1) have been identified as important biomarkers of ischemic pathophysiology (*i.e.*, ischemic-reperfusion response and acute kidney injury, respectively).[40,41] Thus, we next quantified the levels of HSP-70 and KIM-1 in the microfluidic biopsy samples. Additionally, we also quantified the levels of β-actin to assess the metabolic activity of organs throughout the ischemic interval. As shown in Fig. 4f, we found

HSP-70 present in the microfluidic biopsy samples acquired from each experimental group. However, the concentration of HSP-70 varied significantly among the experimental groups ($p_{\text{NT } vs. \text{ HT-P}} = 0.006$; $p_{\text{NT } vs. \text{ HT}} = 0.283$; $p_{\text{HT } vs. \text{ HT-P}} = 0.018$).

For example, the concentration of the HSP-70 was 25, 82 and 409 pg mL^{-1} for the normothermic group (n = 19 organs), the traditional cold storage hypothermic group (n = 6 organs), and the machine-perfused hypothermic group (n = 7 organs), respectively. The observation that hypothermia induces HSP expression in kidney tissue is consistent with previous work.[42,43] For example, it was previously shown that hypothermia induced a 4-fold increase in HSP mRNA levels in mouse kidney tissue,[43] which compares reasonably with the approximate 3-fold increase observed in the microfluidic biopsy samples isolated by the 3D printed device. As shown in Fig. S11 of ESI† KIM-1 and β-actin were also detected in the microfluidic biopsy samples at ranges of 7–12 pg mL^{-1} and 0–7 pg mL^{-1}, respectively; however, no significant differences in the levels among the three groups was observed. The results in Fig. 4 indicate multiple critical findings: 1) whole organs remain metabolically active throughout the clinically relevant ischemic interval; 2) differences in molecular clustering profiles correlate with differences in biomarker expression levels; 3) microfluidic biopsy provides a new technique for isolating biomarkers from whole organs throughout the clinically relevant ischemic interval; and 4) microfluidic biopsy samples have rich diagnostic and assessment value for objective organ assessment, and contain biomarkers of ischemic pathophysiology and metabolic activity.

Conclusions

New devices and techniques for continuously isolating biomarkers from whole organs have the potential to shift the paradigm for the study and analysis of organs as well as help relieve the organ shortage crisis. Here we showed, for the first time, a new technique for isolating molecular species and biomarkers from whole organs *via* 3D printed organ-conforming microfluidic devices, which we refer to as 'microfluidic biopsy'. We found that the molecular clustering profiles of samples isolated by the conformal microfluidic device differ depending on the ischemic conditions of organ preservation. We also found that differences among molecular clustering profiles correlate with differential levels of biomarker expression. Importantly, the samples isolated by the 3D printed organ-conforming microfluidic device contained biomarkers of ischemic pathophysiology and metabolic activity. Thus, the samples isolated by the conformal microfluidic device contain rich diagnostic information. Overall, organ-conforming microfluidic devices represent a new biological technology for objectively assessing the quality of whole organs within the clinically relevant ischemic interval. This work also represents a major advance in microfluidics and device-organ interface through the direct coupling of microfluidics to the surfaces of whole organs. As a result, this work offers new opportunities for assessing, monitoring, and controlling organ health, and therefore, appears poised to help relieve the organ shortage crisis.

Author contributions

YT, KW, MS and SL digitized the whole organ and device topography. MS, APH and BNJ conceived of the 3D printing approach and fabricated the devices. MS, EC, APH and SL characterized the devices. MS, YT and KW performed the microfluidic biopsy studies. KW and BC performed the Raman molecular cluster analysis. RSS, JLR and BNJ designed the Raman spectroscopy studies. KW, CHA and TJO performed organ procurement and preservation. MS, YT and BNJ conducted the computational modeling studies. JLR and BNJ designed the animal studies. JLR and BNJ conceived the microfluidic biopsy concept. MS, YT, KW, BC, TJO and BNJ wrote the manuscript. All authors contributed to editing and data analysis of the final manuscript.

Acknowledgements

The authors thank Zhenyu (James) Kong and Jia (Peter) Liu for their support. BNJ is grateful for the generous support of the National Science Foundation (CBET-1650601).

References

1 J. J. Adams, E. B. Duoss, T. F. Malkowski, M. J. Motala, B. Y. Ahn, R. G. Nuzzo, J. T. Bernhard and J. A. Lewis, *Adv. Mater.*, 2011, **23**, 1335–1340.

2 Y. L. Kong, I. A. Tamargo, H. Kim, B. N. Johnson, M. K. Gupta, T. W. Koh, H. A. Chin, D. A. Steingart, B. P. Rand and M. C. McAlpine, *Nano Lett.*, 2014, **14**, 7017–7023.

3 J. T. Muth, D. M. Vogt, R. L. Truby, Y. Mengüç, D. B. Kolesky, R. J. Wood and J. A. Lewis, *Adv. Mater.*, 2014, **26**, 6307–6312.

4 B. N. Johnson, K. Z. Lancaster, G. Zhen, J. He, M. K. Gupta, Y. L. Kong, E. A. Engel, K. D. Krick, A. Ju, F. Meng, L. W. Enquist, X. Jia and M. C. McAlpine, *Adv. Funct. Mater.*, 2015, **25**, 6205–6217.

5 B. N. Johnson, K. Z. Lancaster, I. B. Hogue, F. Meng, Y. L. Kong, L. W. Enquist and M. C. McAlpine, *Lab Chip*, 2016, **16**, 1393–1400.

6 M. K. Gupta, F. Meng, B. N. Johnson, Y. L. Kong, L. Tian, Y.-W. Yeh, N. Masters, S. Singamaneni and M. C. McAlpine, *Nano Lett.*, 2015, **15**, 5321–5329.

7 A. K. Au, W. Huynh, L. F. Horowitz and A. Folch, *Angew. Chem., Int. Ed.*, 2016, **55**, 3862–3881.

8 C. I. Rogers, K. Qaderi, A. T. Woolley and G. P. Nordin, *Biomicrofluidics*, 2015, **9**, 016501.

9 B. Johnson, K. Lancaster, I. B. Hogue, F. Meng, Y. L. Kong, L. Enquist and M. McAlpine, *Lab Chip*, 2016, **16**, 1393–1400.

10 P. J. Kitson, M. H. Rosnes, V. Sans, V. Dragone and L. Cronin, *Lab Chip*, 2012, **12**, 3267–3271.

11 G. Comina, A. Suska and D. Filippini, *Lab Chip*, 2014, **14**, 424–430.

12 W. Lee, D. Kwon, W. Choi, G. Y. Jung, A. K. Au, A. Folch and S. Jeon, *Sci. Rep.*, 2015, **5**, 7717.

13 S. N. Bhatia and D. E. Ingber, *Nat. Biotechnol.*, 2014, **32**, 760–772.

14 D. J. Beebe, D. E. Ingber and J. den Toonder, *Lab Chip*, 2013, **13**, 3447–3448.

15 A. P. Haring, H. Sontheimer and B. N. Johnson, *Stem Cell Rev. Rep.*, 2017, DOI: 10.1007/s12015-017-9738-0.

16 D. Huh, D. C. Leslie, B. D. Matthews, J. P. Fraser, S. Jurek, G. A. Hamilton, K. S. Thorneloe, M. A. McAlexander and D. E. Ingber, *Sci. Transl. Med.*, 2012, **4**, 159ra147.

17 I. Wagner, E.-M. Materne, S. Brincker, U. Sussbier, C. Fradrich, M. Busek, F. Sonntag, D. A. Sakharov, E. V. Trushkin, A. G. Tonevitsky, R. Lauster and U. Marx, *Lab Chip*, 2013, **13**, 3538–3547.

18 Y. L. Kong, I. Tamargo, H. Kim, B. N. Johnson, M. K. Gupta, T.-W. Koh, H.-A. Chin, D. A. Steingart, B. P. Rand and M. C. McAlpine, *Nano Lett.*, 2014, **14**, 7017–7023.

19 J. A. Paulsen, M. Renn, K. Christenson and R. Plourde, *Printing conformal electronics on 3D structures with Aerosol Jet technology, Future of Instrumentation International Workshop (FIIW) Proceedings*, 2012.

20 T. Blumenthal, V. Fratello, G. Nino and K. Ritala, *Conformal printing of sensors on 3D and flexible surfaces using aerosol jet deposition, Proc. SPIE 8691, Nanosensors, Biosensors, and Info-Tech Sensors and Systems*, 2013.

21 L. Xu, S. R. Gutbrod, A. P. Bonifas, Y. Su, M. S. Sulkin, N. Lu, H.-J. Chung, K.-I. Jang, Z. Liu, M. Ying, C. Lu, R. C. Webb, J.-S. Kim, J. I. Laughner, H. Cheng, Y. Liu, A. Ameen, J.-W. Jeong, G.-T. Kim, Y. Huang, I. R. Efimov and J. A. Rogers, *Nat. Commun.*, 2014, **5**, 3329.

22 I. Jochmans and C. J. E. Watson, *N. Engl. J. Med.*, 2015, **373**, 477–478.

23 G. M. Abouna, *Transplant. Proc.*, 2008, **40**, 34–38.

24 E. A. Pomfret, R. S. Sung, J. Allan, M. Kinkhabwala, J. K. Melancon and J. P. Roberts, *Am. J. Transplant.*, 2008, **8**, 745–752.

25 C. E. Ruhl, B. Sayer, D. Byrd-Holt and D. Brown, in *Costs of Digestive Diseases*, ed. J. E. Everhart, National Institutes of Health, 2008.

26 S. Mohan, K. Foley, M. C. Chiles, G. K. Dube, R. E. Patzer, S. Pastan, R. J. Crew, D. Cohen and L. Ratner, *Kidney Int.*, 2016, **90**, 157–163.

27 C. U. Niemann, J. Feiner, S. Swain, S. Bunting, M. Friedman, M. Crutchfield, K. Broglio, R. Hirose, J. P. Roberts and D. Malinoski, *N. Engl. J. Med.*, 2015, **373**, 405–414.

28 Y. H. Kim and M. R. Lee, *J. Korean Soc. Transplant.*, 2010, **24**, 159–164.

29 A. O. Ojo, D. Heinrichs, J. C. Emond, J. J. McGowan, M. K. Guidinger, F. L. Delmonico and R. A. Metzger, *Am. J. Transplant.*, 2004, **4**, 27–37.

30 A. E. Pozhitkov, R. Neme, T. Domazet-Loso, B. Leroux, S. Soni, D. Tautz and P. A. Noble, *bioRxiv*, 2016, DOI: 10.1101/058305.

31 T. N. K. Zu, A. I. M. Athamneh, E. Collakova, J. Robertson, T. Hawken, C. Aardema and R. S. Senger, *J. Raman Spectrosc.*, 2015, **46**, 551–558.

32 W. M. Haynes, *CRC Handbook of Chemistry and Physics*, 2017.

33 D. Brune and S. Kim, *Proc. Natl. Acad. Sci. U. S. A.*, 1993, **90**, 3835–3839.

34 D. R. Palleros, L. Shi, K. L. Reid and A. L. Fink, *J. Biol. Chem.*, 1994, **269**, 13107–13114.

35 P. K. Rout, R. Kaushik and N. Ramachandran, *Cell Stress Chaperones*, 2016, **21**, 645–651.

36 F. P. Incropera and D. P. DeWitt, *Fundamentals of Heat and Mass Transfer*, John Wiley & Sons, 3rd edn, 1990.

37 M. R. Hajmohammadi, S. S. Nourazar, A. Campo and S. Poozesh, *Int. J. Heat Fluid Flow*, 2013, **40**, 89–96.

38 M. R. Hajmohammadi, S. Poozesh, M. Rahmani and A. Campo, *Appl. Therm. Eng.*, 2013, **61**, 268–277.

39 V. R. Mas, T. F. Mueller, K. J. Archer and D. G. Maluf, *Expert Rev. Mol. Diagn.*, 2011, **11**, 183–196.

40 J. V. Bonventre, *Kidney Int.*, 1993, **43**, 1160–1178.

41 V. S. Vaidya, M. A. Ferguson and J. V. Bonventre, *Annu. Rev. Pharmacol. Toxicol.*, 2008, **48**, 463–493.

42 J. Preuss, R. Dettmeyer, S. Poster, E. Lignitz and B. Madea, *Forensic Sci. Int.*, 2008, **176**, 248–252.

43 K. E. Cullen and K. D. Sarge, *J. Biol. Chem.*, 1997, **272**, 1742–1746.